Springer

KSME

Journal of Mechanical Science and Technology 33 (1) (2019) 29~40
www.springerlink.com/content/1738-494x(Print)/1976-3824(Online)
DOI 10.1007/s12206-018-1204-7

Characteristics analysis of rotor-rolling bearing coupled system with fit looseness fault and its verification †

Wang Haifei[1,2,*], Guan Xiaoying[3,4], Chen Guo[4], Gong Junjie[1], Yu Liang[1], Yuan Shijie[1] and Zhu Zhida[1]

[1]*College of Mechanical Engineering, Yangzhou University, Yangzhou, 225127, China*
[2]*Department of Mechanical Engineering, University of Bristol, Bristol, BS8 1TH, UK*
[3]*School of Software, Guangdong Food and Drug Vocational College, Guangzhou 510000, China*
[4]*College of Civil Aviation, Nanjing University of Aeronautics and Astronautics, Nanjing, 210016, China*

(Manuscript Received January 30, 2018; Revised June 12, 2018; Accepted August 24, 2018)

Abstract

Outer ring of bearing fit looseness fault is a common fault. Scratch often appears in the inner surface of pedestal. The fit looseness fault mechanism is not clear. For rotor-rolling bearing system with fit looseness fault between rotor-bearing outer ring and pedestal, a rotor coupling dynamic model that the interaction of bearing outer ring and pedestal are considered. This model is different from the universal rubbing model, where the directions of relative motion between rotor and stator are not considered. Numerical integration method is used to obtain the response of the system where the rotor is established by FEM and the bearing outer ring and pedestal are established by lumped mass model. Firstly, modal test results and simulation results were used to verify the correctness of this model. Secondly, the role of tightening torque between bearing outer ring and pedestal is considered, and the response characteristics of bearing and rotor are analyzed when fit looseness fault is considered. Finally, comparing the simulation results with test results, the waveform and spectrum are similar, which verifies the correctness of the fit looseness model. The fit looseness fault characteristics are that the acceleration after noise reduction shows periodic impact, up and down asymmetry, multiple frequencies appear. A method by increasing tightening torque is put forward to control the vibration caused by fit looseness fault.

Keywords: Dynamic model; Autocorrelation; Fit looseness fault; Looseness characteristics; Tightening torques

1. Introduction

Looseness fault is a common fault in rotary machinery. Looseness fault usually can be divided into bolt connection looseness fault and bearing fit looseness fault. Scholars at home and abroad have studied on bolt connection looseness fault gradually. The piecewise nonlinear stiffness model is used to study the bolt connection looseness fault. Chen [1] used piece-wise looseness fault model to study the rotor mass unbalance and looseness of bearing house faults. It is found that looseness fault will increase the amplitude under supercritical speeds. Luo [2] established a nonlinear dynamic model of a two-span elastic rotor-bearing system with coupling faults of piece-wise pedestal looseness and rub-impact support on three plain journal bearing. Nonlinear phenomenon was analyzed. Ma [3] established three dynamic models considering pedestal looseness, rub-impact and coupling fault. Piece-wise linear stiffness model was used to simulate looseness fault. The similarities and differences were compared. He [4] also analyzed the effects of the looseness parameters (looseness clearance and stiffness of the foundation) on its dynamic characteristics. Muszynska et al. [5] studied numerically and experimentally the dynamic behavior of a one-lateral-mode unbalanced and radially side-loaded rotor with either a loose pedestal or with occasional rotor-to-stator rubbing. Ehrich [6] used a simple numerical model of rotor employing a single mass mounted on a massless shaft and a piecewise linear bearing support stiffness to represent the system. The result can replicate the response an individual representative points over a range of sub-, trans- and supercritical high-speed rotor operation. Liu et al. [7] established a dual-disk three-support looseness-rubbing fault of rotor-bearing system. The characteristics of looseness-rubbing coupling fault are investigated. Lu et al. [8] investigated experimentally the vibration characteristics of the system with pedestal looseness. It is found that the system motion contains fractional and multiple harmonic components and the looseness occurs intermittently. Wang et al. [9-12] applied a looseness fault model with piecewise linear stiffness to study a single freedom model and real aero-engine model. The nonlinear response characteristics are investigated. Some experiments were conducted to verify the

*Corresponding author. Tel.: +86 25 84891850
E-mail address: wanghaifei1986318@163.com
† Recommended by Associate Editor Kyoung-Su Park

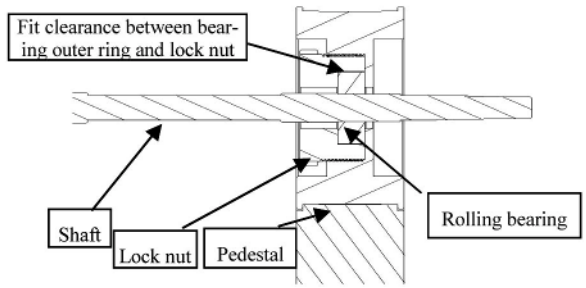

Fig. 1. Sketch of a bearing outer ring and a pedestal at a loose end.

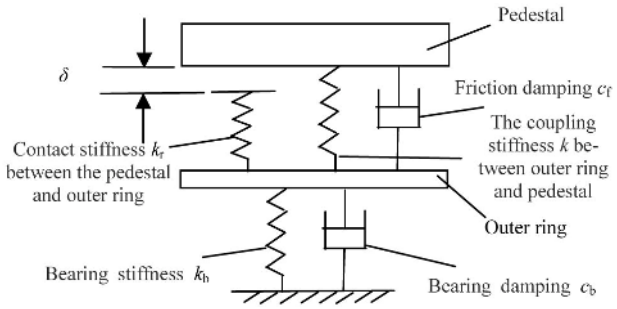

Fig. 2. Physical model of fit looseness fault.

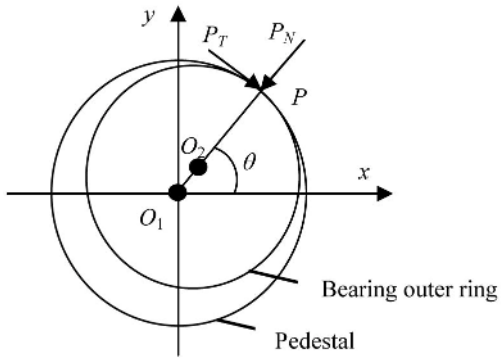

(a) Mechanical diagram

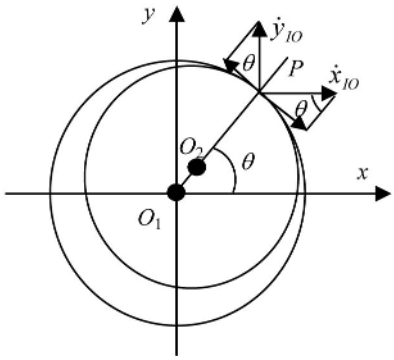

(b) Motion diagram

Fig. 3. A mechanical model with fit looseness fault.

correctness of nonlinear looseness model. Wang [13] studied experimentally the parameters of assembly process of a bearing outer ring and temperature and tightening torque. It is found that the clearance fit and outer ring tightening torque have great influence on the rotor vibration. Chen [14, 15] studied numerically and experimentally the whole vibration of aero-engine. It is found that the proposed model can simulate the natural vibration characteristic of whole aero-engine and perform nonlinear dynamic simulation of whole aero-engine with faults.

Many scholars used piecewise linear stiffness model to represent looseness fault and the nonlinear response mechanism can be obtained by experiments and simulation. However, piecewise linear stiffness model can not be applied to rotating parts with fit looseness fault, the mechanism of rotating parts with fit looseness fault between bearing outer ring and pedestal is not fully studied.

In this paper, a fit looseness fault model between the outer ring and pedestal is established. This model is similar to rubbing fault model, but the big difference is bearing outer ring and pedestal are not rotating and friction force direction needs to be judged and friction effect will be generated between bearing outer ring and pedestal. Then, the fit looseness fault is applied to a rotor-rolling bearing tester, and numerical integration method is used to analyze the influence of fit looseness clearances and tightening torque on response characteristics. Finally, the characteristics of wave and frequency spectrum are compared with certain type of missile turbofan aero-engine vibration, which verified the correctness of the fit looseness model.

2. Modeling of fit looseness fault

2.1 Fit looseness fault model

Fig. 1 is the sketch of a bearing outer ring and a pedestal at a loose end. In this figure, a shaft is supported on a rolling bearing and a lock nut is tightened on the pedestal which is fixed on the ground. Fit clearance exists between the bearing outer ring and the lock nut.

Fig. 2 is the simplified physical fit looseness fault model. Assumed the friction damping is c_f, the connection stiffness between the outer ring and pedestal is k, the contact stiffness of outer ring and pedestal is k_r, bearing stiffness is k_b, and bearing damping is c_b. The nonlinear stiffness will appear in this system when the fit clearance between outer ring and pedestal is less than δ.

Fig. 3 is a mechanical fit looseness model. Fig. 3(a) is the mechanical diagram of bearing outer ring and pedestal. In Fig. 3(a), the center of pedestal is O_1, the center of bearing outer ring is O_2, contact angle position is θ, the normal force is P_N, and tangential force is P_T. Fig. 3(b) is the motion diagram of bearing outer ring and pedestal.

The relative tangential velocity of bearing outer ring and pedestal is decomposed in horizontal and vertical direction. It is assumed that the lateral displacement and velocity of internal bearing outer ring are x_I and $\dot{x}_I$, and the lateral displacement and velocity of external pedestal are x_o and $\dot{x}_o$, so the relative displacement and velocity of bearing outer

ring and pedestal can be described as follows:

$$\begin{cases} x_{IO} = x_I - x_O \\ y_{IO} = y_I - y_O \end{cases} \tag{1}$$

$$\begin{cases} \dot{x}_{IO} = \dot{x}_I - \dot{x}_O \\ \dot{y}_{IO} = \dot{y}_I - \dot{y}_O \end{cases}. \tag{2}$$

It is assumed that the radial displacement of bearing outer ring and pedestal is r, and it can be described as follows:

$$r = \sqrt{(x_I - x_O)^2 + (y_I - y_O)^2}\ . \tag{3}$$

It is assumed that fit clearance between pedestal and bearing outer ring is c. When $r < c$, rubbing will not occur. When $r > c$, bearing outer ring and pedestal will rub, and the angle of contact point P can be described as follows:

$$\begin{cases} \sin\theta = \dfrac{y_{IO}}{r} = \dfrac{y_I - y_O}{r} \\ \cos\theta = \dfrac{x_{IO}}{r} = \dfrac{x_I - x_O}{r} \end{cases}. \tag{4}$$

Assumed that the friction direction of pedestal relative to bearing outer ring at the contact point P is positive in Fig. 3(a), so the tangential velocity of pedestal relative to outer ring can be described as follows:

$$v_T = \dot{y}_{IO}\cos\theta - \dot{x}_{IO}\sin\theta\ . \tag{5}$$

It is assumed that the rubbing of pedestal and bearing outer ring obeys coulomb friction law, so normal force and tangential force generated by rubbing can be described as follows:

$$\begin{cases} P_N = k_r \cdot (r - c) \\ P_T = f \cdot P_N \cdot sign(v_T) \end{cases} \tag{6}$$

where the rubbing stiffness between two fit surfaces is k_r, the friction coefficient is f, and the fit clearance is c. In Eq. (6), tangential friction is not the same as coulomb friction equation, whose direction should be judged by function sign(v_T). The normal collision force and tangential friction force can be divided in x and y axises, and it can be described as follows:

$$\begin{cases} P_x = k_r(1 - c/r)[-(x_I - x_O) + f \cdot sign(v_T) \cdot (y_I - y_O)] \\ P_y = k_r(1 - c/r)[-(y_I - y_O) - f \cdot sign(v_T) \cdot (x_I - x_O)]\ . \end{cases} \tag{7}$$

In Fig. 1, there is fit clearance between bearing outer ring and lock nut, so friction effect on the outer surface of bearing outer ring and inner surface of lock nut appears. Fig. 4 shows the force diagram of the bearing outer ring and lock nut. The fit clearance between the bearing outer ring and lock nut will cause rubbing, and the end friction force of outer ring and lock nut is considered, which is represented by F_y.

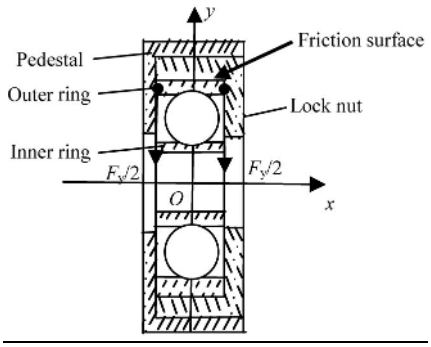

Fig. 4. Force diagram of the bearing outer ring and lock nut.

Assumed that tightening force in the inner surface of the lock nut is F_N, friction coefficient is μ, velocities of bearing outer ring in horizontal and vertical directions at this moment are v_{rx} and v_{ry}. Lock nut is fixed on the pedestal, so the movements of lock nut and pedestal are same. Assumed the velocities of pedestal in horizontal and vertical directions at this moment are v_{bx} and v_{by}. The friction forces at the end surfaces can be described as follows:

$$\begin{cases} F_x = -\mu F_N \operatorname{sign}(v_{rx} - v_{bx}) \\ F_y = -\mu F_N \operatorname{sign}(v_{ry} - v_{by})\ . \end{cases} \tag{8}$$

In this paper, assumed the friction forces are equivalent to viscous damping forces, and the equivalent viscous damping coefficient between bearing outer ring and pedestal is expressed as c_f, as shown in Eq. (9).

$$\begin{cases} F_x = -c_f(v_{rx} - v_{bx}) \\ F_y = -c_f(v_{ry} - v_{by})\ . \end{cases} \tag{9}$$

Obvious nonlinear characteristics will appear in radial directions for the action of rubbing forces between bearing outer ring and pedestal. The friction forces between two contact surfaces will be changed by controlling the tightening torques of pedestal. As the friction forces are equivalent to viscous damping forces, the changing of equivalent viscous damping coefficient can reflect the changing of tightening torques indirectly.

Tightening torques and friction forces between bearing outer ring and pedestal are considered to study the nonlinear response characteristics caused by bearing outer ring and pedestal with fit looseness fault. The rotor-bearing tester is used for simulation analysis.

2.2 Solution of finite element rotor-casing coupling dynamic model

Because the number of DOF in the finite element rotor-support coupling dynamic model is very large, in addition, there

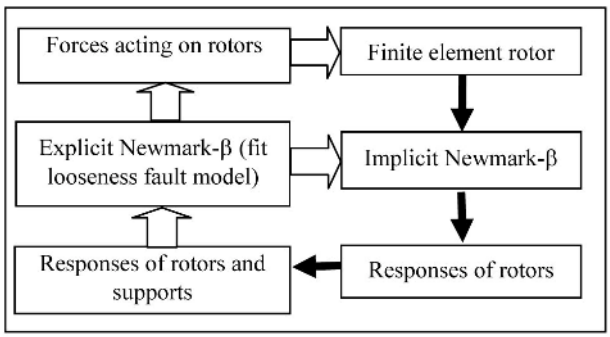

Fig. 5. Solving flow for rotor-support coupling dynamics.

Fig. 6. Physical map of a rotor tester.

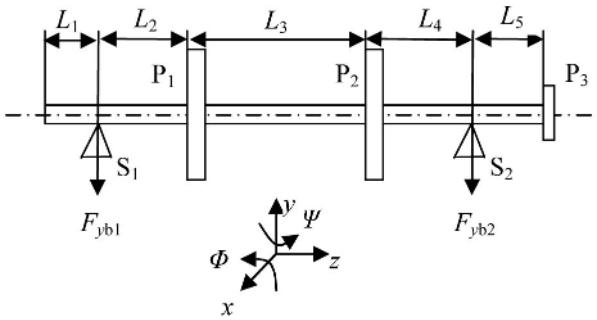

Fig. 7. Rotor model for this tester.

are a lot of strong nonlinear factors, the explicit Newmark-β method and implicit Newmark-β method [9-12] are used to solve system's responses. This finite element rotor-support coupling dynamic solution procedure is shown in Fig. 5.

2.3 The rotor-bearing tester coupling dynamic model

Fig. 6 is the physical map of a rotor tester. Fig. 7 is a rotor model for this tester. Where P_1 , P_2 and P_3 are disk 1, disk 2 and Table 3, respectively; S_1 and S_2 are two ends of the rotor supporting position; F_{yb1} and F_{yb2} are the contact forces between the rotor and support, respectively. In Fig. 6, the mass of disk 1 and disk 2 is 2.4 kg; polar moment of inertia is 0.0125 kg·m^2; equator moment of inertia is 0.00625 kg·m^2; the mass of disk 3 is 1.05 kg; polar moment of inertia is 8×10^{-4} kg·m^2; equator moment of inertia is 4×10^{-4} kg·m^2; the diameter of this shaft is 0.019 m; L_1, L_2, L_3, L_4 and L_5 are 100 mm, 152 mm, 380 mm, 180 mm and 130 mm, respectively.

Table 1. Results of frequency identification.

	The first order	The second order	The third order
Experimental frequency /Hz	44.53	114.37	222.54
Frequency from simulation /Hz	40.15	111.87	214.81

(a) The first three order vibration modes obtained from experiments

(b) The first three order vibration modes from simulation

Fig. 8. The first three order vibration modes from experiments and simulation.

In modal test, the acceleration sensor was installed on the rotor and hammer was used to knock 6 points on the shaft. The method of single measurement point and multiple excitations was adopted, force and acceleration were input to NI collector, and parameter value was obtained by modal software.

Fig. 8 is the comparison of the first three order test vibration modes and calculation vibration modes. Table 1 is the natural frequencies. By comparing the first three order vibration modes and frequencies obtained from experiments and simulation, the modes and frequencies are valid and the model for the tester is correct. Based on this valid model, simulation on different looseness fault conditions is conducted.

3. 1Fit looseness fault simulation

3.1 Simulation conditions

In order to analyze the influence of tightening torques, rotating speeds, radial clearances and friction forces, different fit looseness fault conditions are set to simulate as follows:

(1) The friction effect between bearing outer ring and lock nut is not considered when there is a fit looseness fault. Assumed the fit clearances are 0 μm, 30 μm, 50 μm and 100 μm, the elastic rubbing stiffness at this support is 1×10^6 N/m, line spring stiffness between bearing outer ring and rotor is 1×10^8 N/m, and damping coefficient is 2000 N·s/m.

(2) The friction effect between bearing outer ring and lock nut is considered when there is a fit looseness fault. Assumed the fit clearances are 0 μm, 30 μm, 50 μm and 100 μm, the elastic rubbing stiffness at this support is 1×10^6 N/m, friction coefficient is 0.1, line spring stiffness between bearing outer ring and rotor is 1×10^8 N/m, and damping coefficient is 2000 N·s/m.

(3) The changing of tightening torques can be achieved by changing the viscous damping coefficient. The influence of tightening torques on vibration can be represented by chang-

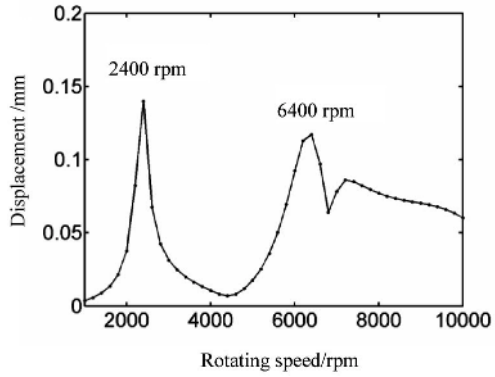

Fig. 9. Bode plot of rotor vibration.

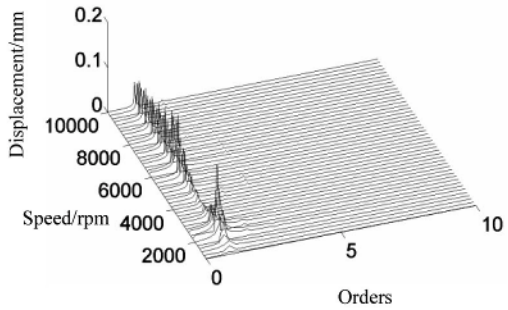

(a) Waterfall plot of rotor lateral displacement

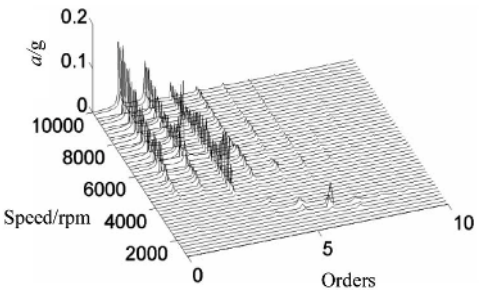

(b) Waterfall plot of pedestal vertical acceleration

Fig. 10. Waterfall plot of rotor lateral displacement and pedestal vertical acceleration when the fit clearance is 30 μm.

ing rotating speeds, radial fit looseness clearances, and friction forces.

(4) The unbalance excitation of three disks is considered, and their eccentricities are 0.3 mm.

(5) The rotating speed range is 1000-10000 rpm.

(6) The measurement points are vertical acceleration on pedestal and rotor displacement.

3.2 Response characteristics analysis regardless of tightening torques

Fig. 9 is the rotor vertical amplitude changing with rotating speeds. As can be seen from this figure, the first two order critical speeds are 2400 rpm and 6400 rpm, respectively.

Figs. 10-12 are the waterfall plot of rotor displacement and pedestal acceleration when the viscous damping is 500 N·s/m,

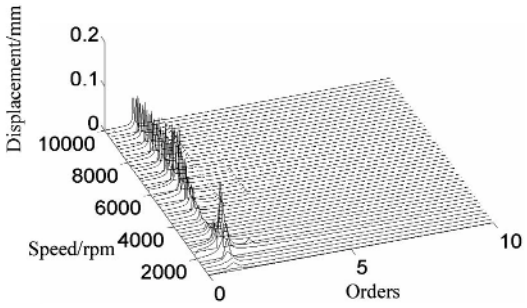

(a) Waterfall plot of rotor lateral displacement

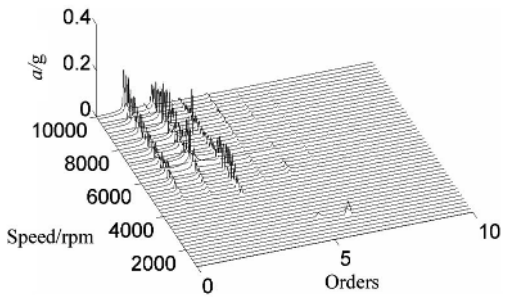

(b) Waterfall plot of pedestal vertical acceleration

Fig. 11. Waterfall plot of rotor lateral displacement and pedestal vertical acceleration when the fit clearance is 50 μm.

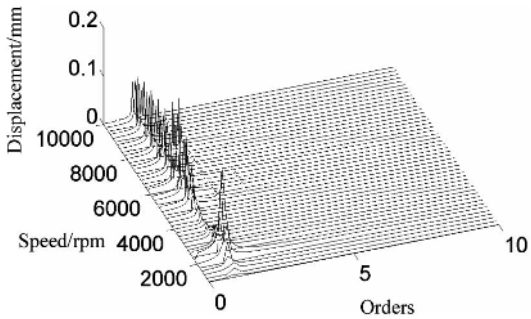

(a) Waterfall plot of rotor lateral displacement

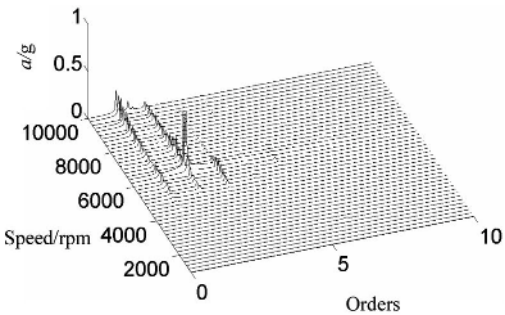

(b) Waterfall plot of pedestal vertical acceleration

Fig. 12. Waterfall plot of rotor lateral displacement and pedestal vertical acceleration when the fit clearance is 100 μm.

fit looseness clearances between outer ring and pedestal are 30 μm, 50 μm and 100 μm, respectively. As can be seen from these figures, multiple frequencies are more obvious with the increase of fit looseness clearances in rotor displacement and pedestal acceleration waterfall plot. Super-harmonic reso-

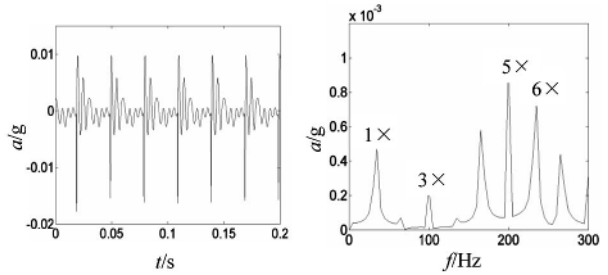

(a) Waveform before noise reduction (b) Spectrum before noise reduction

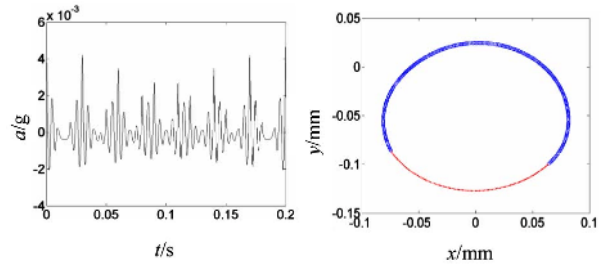

(c) Waveform after noise reduction (d) Orbit

Fig. 13. Pedestal acceleration waveform, spectrum, and rotor orbit when the rotating speed is 2000 rpm.

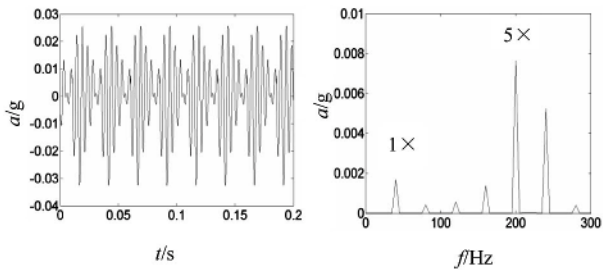

(a) Waveform before noise reduction (b) Spectrum before noise reduction

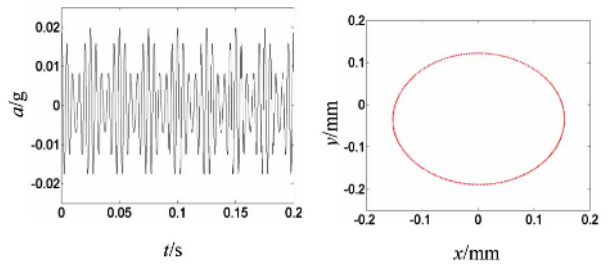

(c) Waveform after noise reduction (d) Orbit

Fig. 14. Pedestal acceleration waveform, spectrum, and rotor orbit when the rotating speed is 2400 rpm.

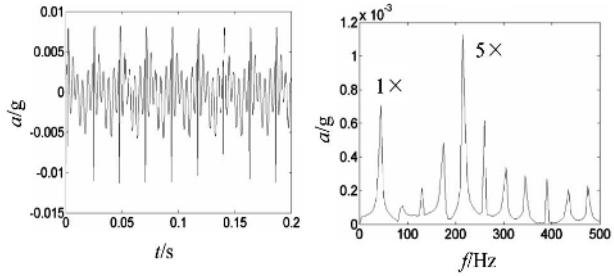

(a) Waveform before noise reduction (b) Spectrum before noise reduction

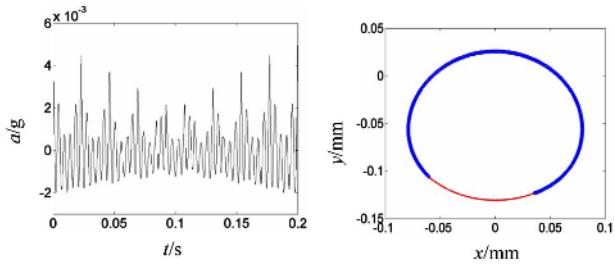

(c) Waveform after noise reduction (d) Orbit

Fig. 15. Pedestal acceleration waveform, spectrum, and rotor orbit when the rotating speed is 2600 rpm.

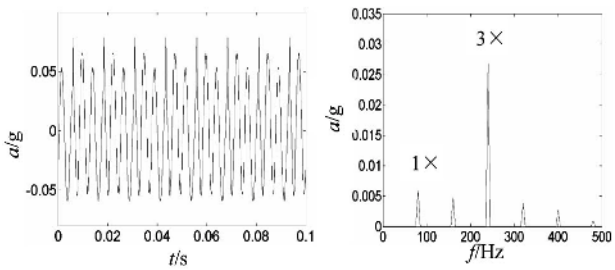

(a) Waveform before noise reduction (b) Spectrum before noise reduction

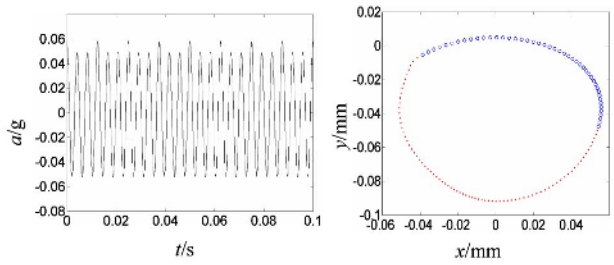

(c) Waveform after noise reduction (d) Orbit

Fig. 16. Pedestal acceleration waveform, spectrum, and rotor orbit when the rotating speed is 4800 rpm.

nance, and multiple frequencies under high rotating speeds are obvious than that under lower rotating speeds. It showed that nonlinearity is strengthening under the higher rotating speeds for rubbing effects.

Figs. 13-18 are the pedestal acceleration waveform, its spectrum before and after noise reduction and the orbit of rotor at the looseness location. The fit clearance is 50 μm and the rotating speeds are 2000 rpm, 2400 rpm, 2600 rpm, 4800 rpm, 6000 rpm and 8400 rpm. Red curve is used when outer ring and pedestal rubs, otherwise, blue curve is used.

In Figs. 13(a) and (c), the acceleration plots show obvious periodic impact phenomenon when the rotating speeds are under the first order critical speed 2400 rpm. In Fig. 13(d), the amplitude of rotor is small, and the rotor is whirling at the bottom. The rubbing time of outer ring and pedestal is short as the fit clearance between outer ring and pedestal is large.

In Fig. 14(c), the pedestal acceleration after noise reduction shows periodic impact, up and down asymmetry, and multiple

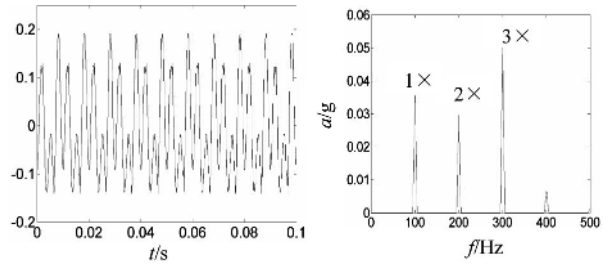

(a) Waveform before noise reduction (b) Spectrum before noise reduction

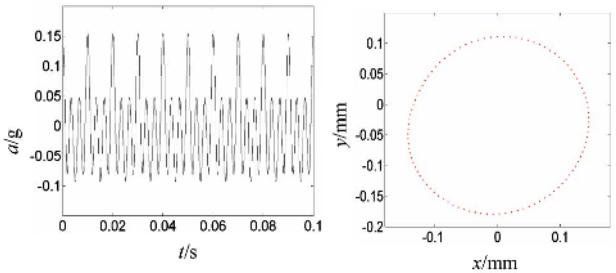

(c) Waveform after noise reduction (d) Orbit

Fig. 17. Pedestal acceleration waveform, spectrum, and rotor orbit when the rotating speed is 6000 rpm.

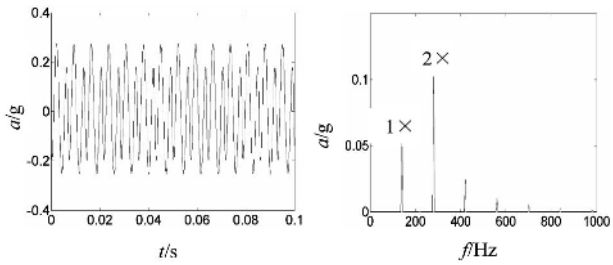

(a) Waveform before noise reduction (b) Spectrum before noise reduction

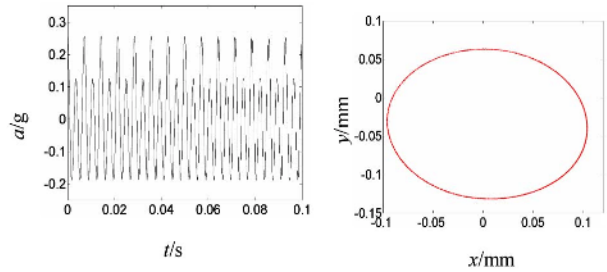

(c) Waveform after noise reduction (d) Orbit

Fig. 18. Pedestal acceleration waveform, spectrum, and rotor orbit when the rotating speed is 8400 rpm.

frequencies appear in Fig. 14(b). In Fig. 14(d), the fit clearance between outer ring and pedestal disappears when the speed is at the first order critical speed 2400 rpm. As the amplitude of rotor is large, that is, the outer ring and pedestal always rub.

In Figs. 15(a) and (c), pedestal acceleration plots after noise reduction show periodic impact and multiple frequencies appear in Fig. 15(b). In Fig. 15(d), when the rotating speed has passed the first order critical speed 2400 rpm, the amplitude of rotor has been decreased, the rubbing time is shorter and the rotor is whirling at the bottom.

In Figs. 16(a) and (c), pedestal acceleration plots after noise reduction show periodic impact and multiple frequencies appear in Fig. 16(b). In Fig. 16(d), the amplitude of rotor has been increased, the rubbing time is longer.

In Figs. 17(c) and 18(c), pedestal acceleration plots after noise reduction show obvious periodic impact, up and down asymmetry, and multiple frequencies appear in Figs. 17(b) and 18(b). In Figs. 17(d) and 18(d), the fit clearances between outer ring and pedestal disappear, and the outer ring and pedestal always rub.

In these figures, super-harmonic resonance appears obviously, that is, 6× in Fig. 13(b), 5× in Fig. 14(b), 3× in Fig. 16(b) and 2× in Fig. 18(b).

3.3 Response characteristics analysis considering tightening torques

In order to analyze the influence of the tightening torques on the response of rotor system, the response of the rotor system is obtained by simulation. The viscous damping is increased from 500 N.s/m to 1000 N·s/m and fit clearances are

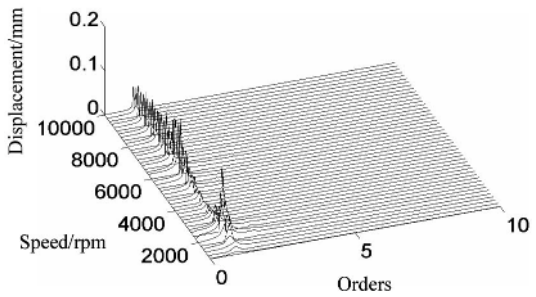

(a) Waterfall plot of rotor lateral displacement

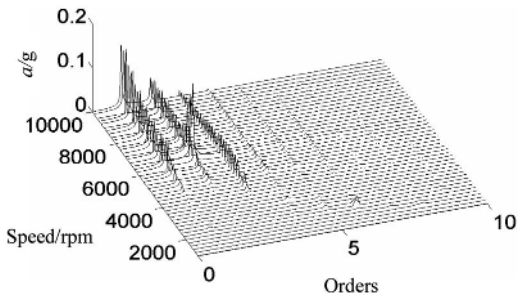

(b) Waterfall plot of pedestal vertical acceleration

Fig. 19. Waterfall plot of rotor lateral displacement and pedestal vertical acceleration when fit clearance is 30 μm.

30 μm, 50 μm and 100 μm, respectively. The results are shown in Figs. 19-21. It is found that multiple frequencies under different rotating speeds are not obvious in the waterfall plot of pedestal acceleration with the increase of tightening torques, comparing with Figs. 10-12. Nonlinear phenomenon becomes less obvious by increasing the tightening torques.

Figs. 22 and 23 are the waveform, spectrum of pedestal acceleration before and after noise reduction and rotor orbit. The

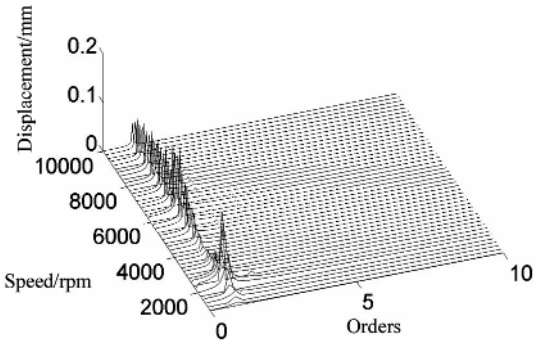

(a) Waterfall plot of rotor lateral displacement

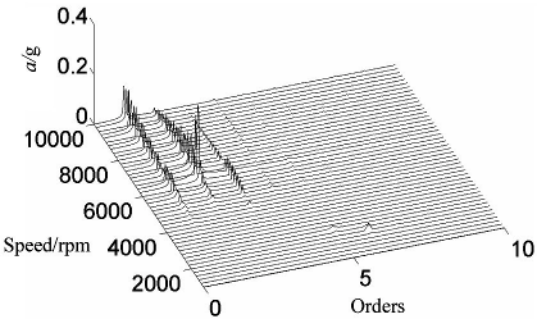

(b) Waterfall plot of pedestal vertical acceleration

Fig. 20. Waterfall plot of rotor lateral displacement and pedestal vertical acceleration when fit clearance is 50 μm.

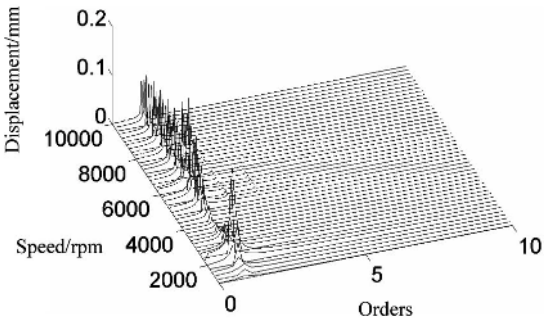

(a) Waterfall plot of rotor lateral displacement

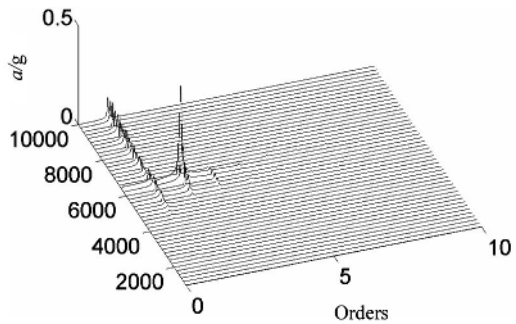

(b) Waterfall plot of pedestal vertical acceleration

Fig. 21. Waterfall plot of rotor lateral displacement and pedestal vertical acceleration when fit clearance is 100 μm.

rotating speed is 2400 rpm, fit clearance is 50 μm, viscous damping are 1600 N·s/m and 3000 N·s/m, respectively. As can

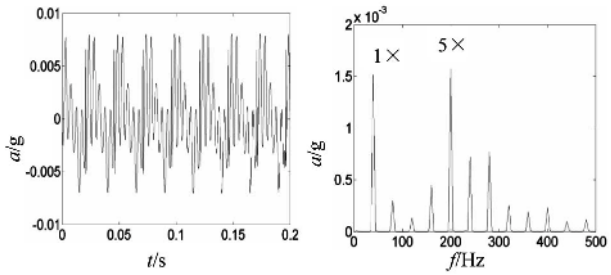

(a) Waveform before noise reduction (b) Spectrum before noise reduction

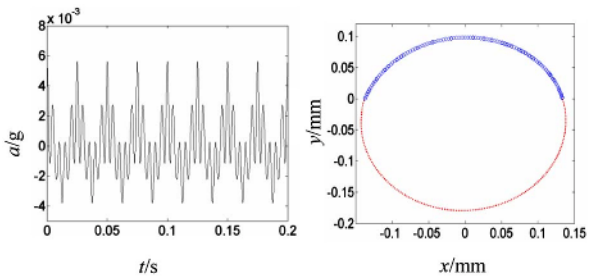

(c) Waveform after noise reduction (d) Orbit

Fig. 22. Pedestal acceleration waveform, spectrum, and rotor orbit when the rotating speed is 2400 rpm and viscous damping is 1600 N·s/m.

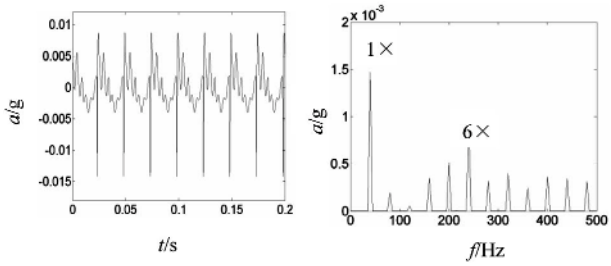

(a) Waveform before noise reduction (b) Spectrum before noise reduction

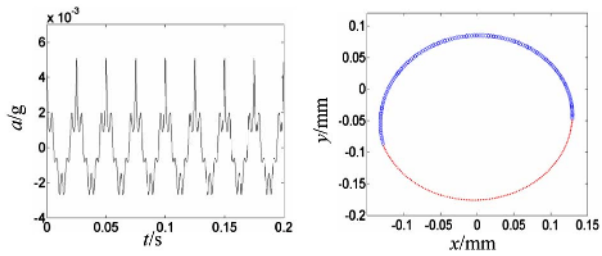

(c) Waveform after noise reduction (d) Orbit

Fig. 23. Pedestal acceleration waveform, spectrum, and rotor orbit when rotating speed is 2400 rpm and viscous damping is 3000 N·s/m.

be seen from these figures, the rotating speed is at the critical speed 2400 rpm, so the vibration displacements are larger and it is difficult to make collision and friction effect disappeared by increasing the tightening torques between bearing outer ring and pedestal.

Figs. 24-26 are the waveform, spectrum of pedestal acceleration before and after noise reduction and rotor orbit. The rotating speed is 10000 rpm, fit clearance is 50 μm, and viscous damping are 1000 N·s/m, 1600 N·s/m and 3000 N·s/m,

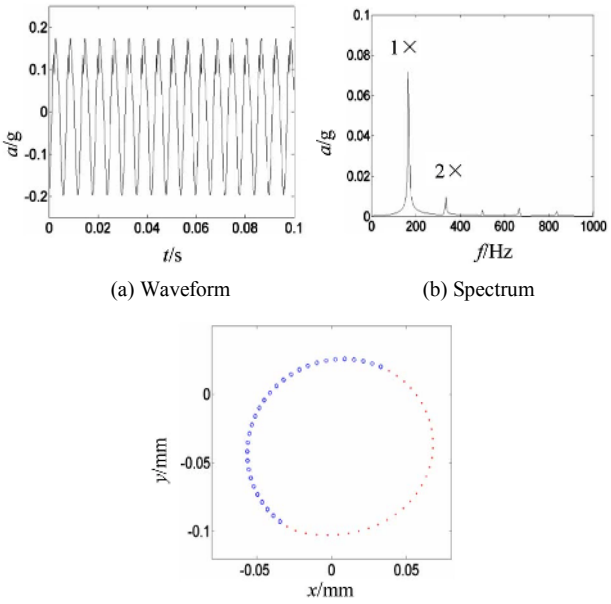

(a) Waveform (b) Spectrum

(c) Orbit

Fig. 24. Pedestal acceleration waveform, spectrum, and rotor orbit when rotating speed is 10000 rpm and viscous damping is 1000 N·s/m.

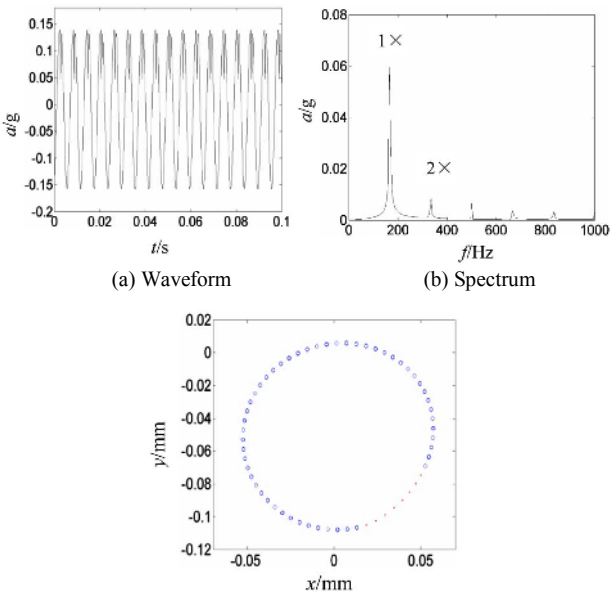

(a) Waveform (b) Spectrum

(c) Orbit

Fig. 25. Pedestal acceleration waveform, spectrum, and rotor orbit when rotating speed is 10000 rpm and viscous damping is 1600 N·s/m.

respectively. As can be seen from these figures, the rotating speed is not at the critical speed 2400 rpm, so the vibration displacement is smaller, it is easy to make collision and friction effect disappeared by increasing the tightening torques between bearing outer ring and pedestal.

3.4 Verification of test data

Fig. 27 is certain types of missile turbofan No. Z09077

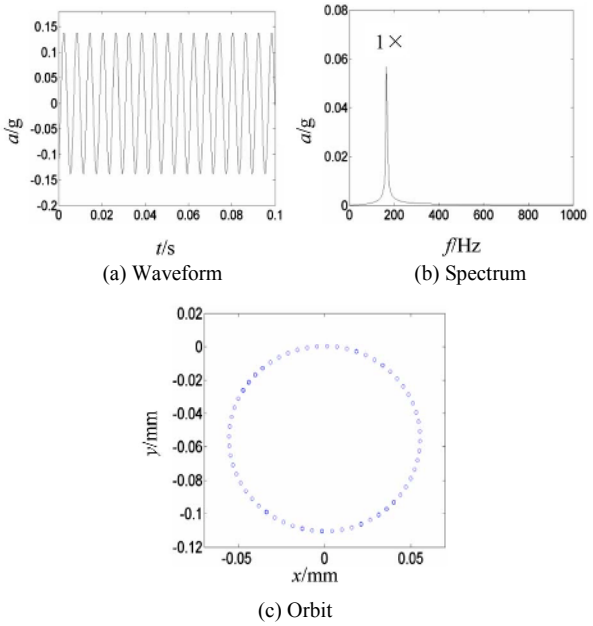

(a) Waveform (b) Spectrum

(c) Orbit

Fig. 26. Pedestal acceleration waveform, spectrum, and rotor orbit when rotating speed is 10000 rpm and viscous damping is 2400 N·s/m.

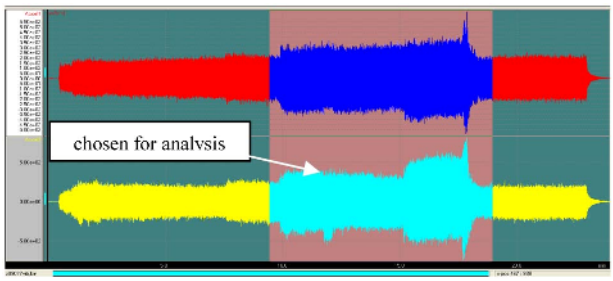

Fig. 27. Test data.

aero-engine test data. The aero-engine's radial vibrations are measured by two acceleration sensors, one of which is installed on the aero-engine's lateral horizontal position and the other, on the aero-engine's top vertical position. The sampling frequency is 12.8 kHz. During the trial running process, the whole aero-engine vibration value often exceeds the standard limit and 550 seconds is chosen for analysis.

Figs. 28 and 29 are horizontal and vertical acceleration changing with time. It show 1×, 2×, 3×, 4× components and RMS of casing acceleration change with time. In Fig. 28, 1× is dominant during 0 s-550 s, the horizontal acceleration increases rapidly when the rotating speed is around 33187 rpm and 3× increases rapidly. However, in Fig. 29, 3× and 4× are dominant during 0 s-550 s, and 1×, 2×, 3× and 4× increase rapidly when the rotating speed is around 33187 rpm.

Fig. 30 is the rotating speeds changing with time. It shows the starting time from 0 s to 500 s and closing time from 500 s to 550 s. Figs. 31(a) and (b) are 1× of horizontal and vertical acceleration at rotating speeds from 30000 rpm to 33000 rpm. In Fig. 31(a), 1× of horizontal acceleration increases rapidly from 6 g to 15 g when the rotating speeds were changing from

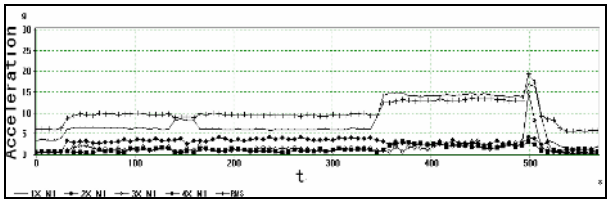

Fig. 28. Horizontal acceleration changing with time.

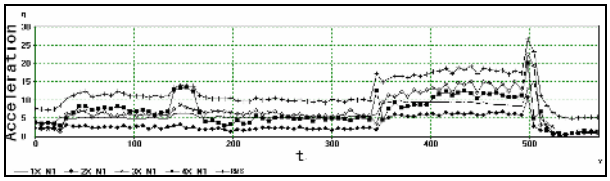

Fig. 29. Vertical acceleration changing with time.

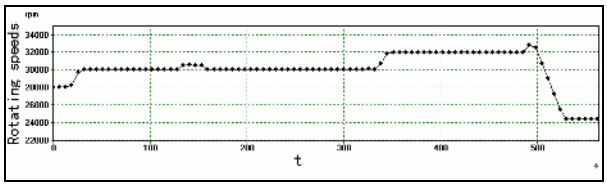

Fig. 30. Speeds changing with time.

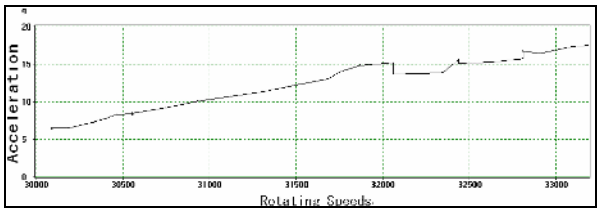

(a) Horizontal acceleration

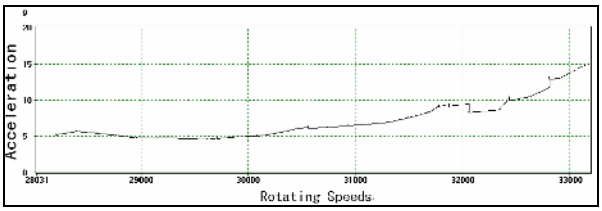

(b) Vertical acceleration

Fig. 31. Acceleration amplitude changing with rotating speeds.

30000 rpm to 32000 rpm, and it keeps increasing from 15 g to 18 g when the rotating speeds were changing from 32000 rpm to 33000 rpm. In Fig. 31(b), 1× of vertical acceleration increases slightly from 5 g to 9 g when the rotating speeds were changing from 30000 rpm to 32000 rpm and it keeps increasing from 9 g to 15 g when the rotating speeds were changing from 32000 rpm to 33000 rpm.

Figs. 32(a) and (b) are the waterfall plot of vibration data. As can be seen from the waterfall plot of horizontal acceleration, 1× is obvious when the rotating speeds are under 33187 rpm. However, 3× is more obvious when the rotating speed is around 33187 rpm. In the vertical acceleration, 2×, 3× and 4× are obvious.

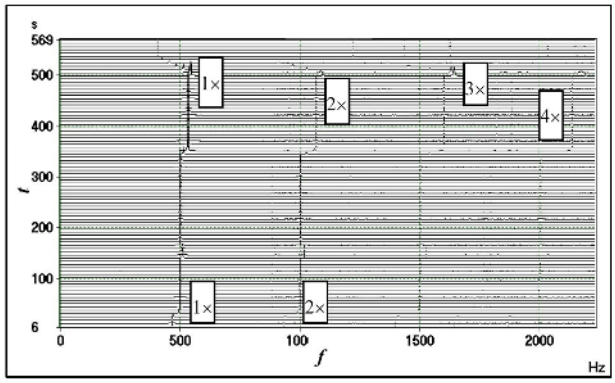

(a) Horizontal acceleration spectrum

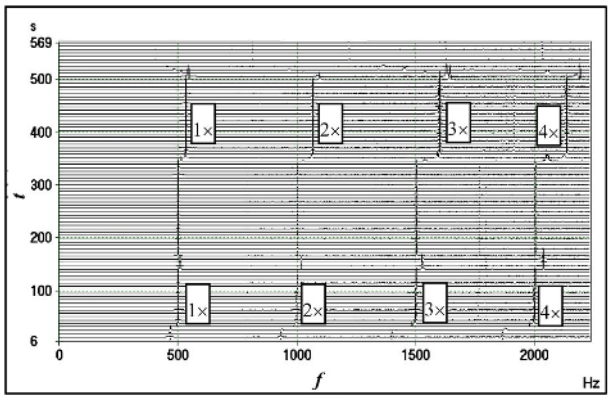

(b) Vertical acceleration spectrum

Fig. 32. Waterfall plot of horizontal and vertical acceleration.

Figs. 33 and 34 are the waveform and spectrum of horizontal and vertical acceleration after noise reduction when the rotating speeds are 31968 rpm and 32812 rpm. In Fig. 33, 1× is more obvious than other frequency components in horizontal direction. However, 2×, 3× and 4× become more obvious in vertical direction. The waveform shows periodic impact, up and down asymmetry. The wave is the same as Fig. 23(c) shown in Fig. 33(e). In Fig. 34, 3× is obvious in horizontal direction. The wave is same as Fig. 22(c) shown in Fig. 34(e). However, 3× is more obvious in vertical direction. The wave is the same as Fig. 17(c) shown in Fig. 34(f).

4. Conclusion

By comparing the waveform of test data with the waveform from real rotor vibration model, some results can be acquired as follows:

(1) A dynamic model of a rotor tester with fit looseness fault was established, modal test was used for verification, and the fit looseness simulation is carried out under different fit looseness clearances.

(2) The acceleration response of pedestal was obtained. It can be found that pedestal acceleration after noise reduction showed periodic impact, up and down asymmetry, multiple frequencies appeared. The influence of tightening torques on

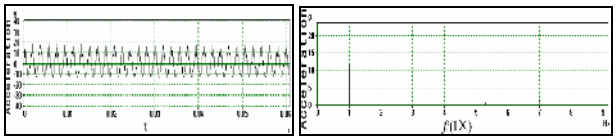

(a) Waveform (horizontal direction) (b) Spectrum

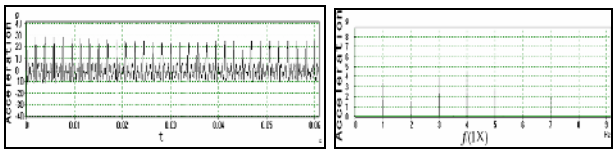

(c) Waveform (vertical direction) (d) Spectrum

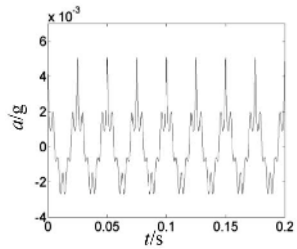

(e) Waveform after noise reduction

Fig. 33. Waveform and spectrum of acceleration when the rotating speed is 31968 rpm.

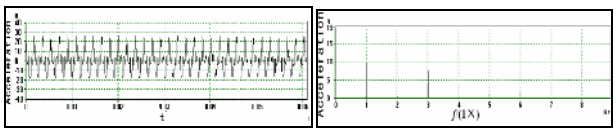

(a) Waveform (horizontal direction) (b) Spectrum

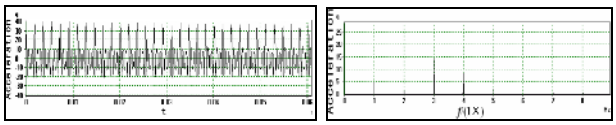

(c) Waveform (vertical direction) (d) Spectrum

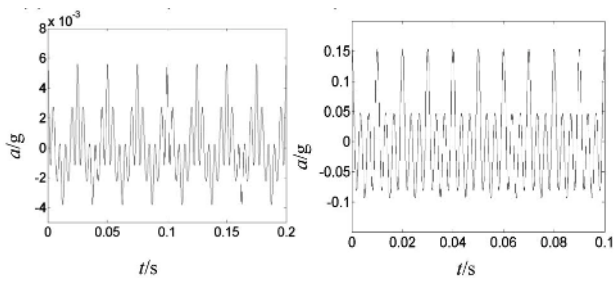

(e) Waveform after noise reduction (f) Waveform after noise reduction

Fig. 34. Waveform and spectrum of acceleration when the rotating speed is 32812 rpm.

the response of pedestal was analyzed. Vibration can be suppressed by increasing tightening torques.

(3) By comparing the simulation with test data, the fault vibration waveform from simulation and test were same. Acceleration after noise reduction showed periodic impact, up and down asymmetry, multiple frequencies appeared. This characteristics can indicate that fit looseness fault exists. By decomposing the engine, it can be found that wear phenomenon appear in bearing outer ring which showed that fit looseness fault existed. The characteristics can provide qualitative judgment for engine with fit looseness fault.

Acknowledgments

This work is supported by Chinese Scholarship Council with Granted No. 201708320058 and Funding of Scientific and Technological Innovation cultivating Program of Yangzhou University 2017CXJ022, Jiangsu Province Basic Research Program (Grant No. BK20160474) and Natural science fund for colleges and universities in Jiangsu Province (Grant No. 16KJB460024).

References

[1] G. Chen, Nonlinear dynamics of unbalance-looseness coupling faults of rotor-ball bearing-stator coupling system, *Journal of Mechanical Engineering*, 44 (3) (2008) 82-88 (in Chinese).

[2] Y. G. Luo et al., Nonlinear characteristics of two-span rotor-bearing system with coupling faults of pedestal looseness and rub-impact, *Transactions of the Chinese Society for Agricultural Machinery*, 39 (11) (2008) 180-183 (in Chinese).

[3] H. Ma et al., Dynamic characteristic analysis of a rotor system with pedestal looseness coupled rub-impact fault, *Journal of Mechanical Engineering*, 48 (19) (2012) 80-86 (in Chinese).

[4] H. Ma et al., Analysis of dynamic characteristics for a rotor system with pedestal looseness, *Shock and Vibration*, 18 (1) (2011) 13-27.

[5] A. Muszynska and P. Goldman, Chaotic responses of unbalanced rotor bearing stator systems with looseness or rubs, Chaos, *Solitons and Fractals*, 5 (9) (1995) 1683-1704.

[6] F. F. Ehrich, A new class of asynchronous rotordynamic response in high-speed rotors, *Proc. of the ASME 2007 Design Engineering Technical Conferences & Computers and Information in Engineering Conference*, Las Vegas, Nevada, USA (2007).

[7] Y. Liu et al., Looseness-rubbing coupling fault of dual-disk three-supporting rotor-bearing system, *Journal of Aerospace Power*, 28 (5) (2013) 977-982 (in Chinese).

[8] W. Lu and F. Chu, Experimental investigation of pedestal looseness in a rotor-bearing system, *Key Engineering Materials* (2009) 413-414, 599-605.

[9] H. F. Wang and G. Chen, Certain type turbofan engine whole vibration model with support looseness fault and casing response characteristics, *Shock and Vibration* (2014) 1-23.

[10] H. F. Wang, G. Chen and P. P. Song, Asynchronous vibration response characteristics of connectors with looseness fault and its verification, *Journal of Vibroengineering*, 17 (7) (2015) 3551-3560.

[11] H. F. Wang, G. Chen and P. P. Song, Asynchronous vibration response characteristics of aero-engine with support looseness fault, *Journal of Computational and Nonlinear Dynamics* (2016) 11:031013-1-031013-10.
[12] H. F. Wang et al., Modeling for whole missile turbofan engine vibration with support looseness fault and characteristics of casing response, *Journal of Aerospace Power*, 30 (3) (2015) 627-638 (in Chinese).
[13] S. J. Wang et al., Nonlinear vibration of rotor systems caused by assembly process of a bearing outer ring of an aero-engine, *Journal of Aerospace Power*, 30 (1) (2015) 82-89 (in Chinese).
[14] G. Chen, A coupling dynamic model for whole aero-engine vibration and its verification, *Journal of Aerospace Power*, 27 (2) (2012) 242-254 (in Chinese).
[15] G. Chen, Vibration modeling and verifications for whole aero-engine, *Journal of Sound and Vibration*, 349 (4) (2015) 163-176.

Wang Haifei is a lecturer of College of Mechanical Engineering, Yangzhou University, Yangzhou, P. R. China. He is currently mainly engaged in the study of whole aero-engine vibration, rotating machine fault diagnosis, aerodynamics, acoustics, UAV noise prediction.
E-mail: wanghaifei1986318@163.com

Guan Xiaoying received a master degree in the School of Software from the Sun Yat-sen University, Guangzhou, P. R. China, in 2008. Now she is a student in the College of Civil Aviation, Nanjing University of Aeronautics and Astronautics, Nanjing, P. R. China. Her current research interests include genetic algorithm, pattern recognition and machine learning, and their application in bearing fault diagnosis.

Chen Guo is a Professor at the College of Civil Aviation, Nanjing University of Aeronautics and Astronautics, Nanjing, P. R. China. He is currently mainly engaged in the study of whole aero-engine vibration, rotor-bearing dynamics, rotating machine fault diagnosis, pattern recognition and machine learning, and signal analysis and processing.
E-mail: cgzyx@263.net

Gong Junjie is a Professor of College of Mechanical Engineering, Yangzhou University, Yangzhou, P. R. China. He is currently mainly engaged in the study of the dynamic and static test and optimization of the mechanical structure, and computer modeling and simulation of engineering problems.
E-mail: gjunj@126.com

Yu Liang is a lecturer of College of Mechanical Engineering, Yangzhou University, Yangzhou, P. R. China. He is currently engaged in the fields of tribology of surface engineering, mechanical dynamics, and numerical simulation.
E-mail: yuliang@yzu.edu.cn

Yuan Shijie is a mechanical engineer of College of Mechanical Engineering, Yangzhou University, Yangzhou, P. R. China. He is currently mainly engaged in the study of mechanical design and metal processing technology.
E-mail: 006478@yzu.edu.cn

Zhu Zhida is a senior engineer of College of Mechanical Engineering, Yangzhou University, Yangzhou, P. R. China. He is currently mainly engaged in the study of magnetic motor design and mechanical working.
E-mail: zdzhu@yzu.edu.cn